AD_____

Award Number: DAMD17-99-1-9121

TITLE: Improved MR Images of Breast Lesions with Fast Spectroscopic Imaging

PRINCIPAL INVESTIGATOR: Gregory S. Karczmar, Ph.D.

CONTRACTING ORGANIZATION: The University of Chicago
Chicago, Illinois 60637

REPORT DATE: October 2000

TYPE OF REPORT: Annual

PREPARED FOR: U.S. Army Medical Research and Materiel Command
Fort Detrick, Maryland 21702-5012

REPORT DOCUMENTATION PAGE

Form Approved
OMB No. 074-0188

1. AGENCY USE ONLY (Leave blank)	2. REPORT DATE	3. REPORT TYPE AND DATES COVERED
	October 2000	Annual (15 Sep 99 – 14 Sep 00)

4. TITLE AND SUBTITLE

Improved MR Imaging of Breast Lesions with Fast Spectroscopic Imaging

5. FUNDING NUMBERS

DAMD17-99-1-9121

6. AUTHOR(S)

Gregory S. Karczmar, Ph.D.

7. PERFORMING ORGANIZATION NAME(S) AND ADDRESS(ES) University of Chicago

The University of Chicago
Chicago, Illinois 60637
E-Mail:gskarczm@midway.uchicago.edu

8. PERFORMING ORGANIZATION REPORT NUMBER

9. SPONSORING / MONITORING AGENCY NAME(S) AND ADDRESS(ES)

U.S. Army Medical Research and Materiel Command
Fort Detrick, Maryland 21702-5012

10. SPONSORING / MONITORING AGENCY REPORT NUMBER

11. SUPPLEMENTARY NOTES

12a. DISTRIBUTION / AVAILABILITY STATEMENT

Approved for Public Release; Distribution Unlimited

12b. DISTRIBUTION CODE

13. ABSTRACT *(Maximum 200 Words)*

The progress to date suggests that HiSS can be successfully implemented on clinical scanners and produce high quality images which contain information that is not available in conventional MR scans. HiSS MRI is particularly useful for detection of contrast agents. It is likely that HiSS will produce a significant increase in sensitivity and specificity of MRI for detection of breast cancer as well as other cancers. This means that cancers can be detected early when they are highly treatable. Earlier cancer detection is likely to improve clinical outcome for many cancer patients.

During the next year of support we plan to continue to optimize HiSS MRI on the clinical scanner. At the same time, we will begin to scan patients with breast cancer to determine whether HiSS MRI provides significant increases in the sensitivity and accuracy of cancer detection and staging. We believe that based on the difficulty of optimizing HiSS data acquistion and analysis on clinical scanners, a limited amount of work using animal model tumors as a 'test bed' continues to be justified.

14. SUBJECT TERMS

15. NUMBER OF PAGES 40

16. PRICE CODE

17. SECURITY CLASSIFICATION OF REPORT	18. SECURITY CLASSIFICATION OF THIS PAGE	19. SECURITY CLASSIFICATION OF ABSTRACT	20. LIMITATION OF ABSTRACT
Unclassified	Unclassified	Unclassified	Unlimited

NSN 7540-01-280-5500

Standard Form 298 (Rev. 2-89)
Prescribed by ANSI Std. Z39-18
298-102

Table of Contents

(2) **INTRODUCTION:** *Narrative that briefly (one paragraph) describes the subject, purpose, and scope of the research.*

The goal of this research is to use high spectral and spatial resolution (HiSS) MR imaging to improve images of human breast. Specifically, we expect to 1) improve separation of water and fat signals 2) increase image contrast 3) improve detection of suspicious lesions such as cancers and particularly delineation of tumor edges 4) increase sensitivity to contrast agents and to local physiology. As a result, we hope to increase the sensitivity and specificity of MR scans for breast cancer. To achieve these goals our original 'statement of work' (**SOW**) was as follows:

A. Implementation of FSI methods on a clinical Scanner: Our clinical whole body scanners will be programmed to produce oscillating gradients during the decay of the proton FID so that a series of gradient echoes can be detected following excitation.

B. Processing FSI Data: Spectral information in FSI data sets will be analyzed to reduce the effects of resonance offset in MR images. Then the corrected FSI data will be used to synthesize images in which intensity is proportional to the peak intensity, linewidth, integral, and resonance frequency of resonances.

C. A phantom which contains large magnetic susceptibility gradients and both lipid and water compartments will be constructed to allow evaluation and optimization of FSI methods. Conventional spectroscopic images which use only phase encoding gradients to obtain spatial information will provide 'gold standard' images of the phantom.

D. Studies of patients: Women who are at increased risk for breast ca ncer and attend our 'high risk' clinic, and patients who are treated with neoadjuvant therapy for breast cancer will be recruited for MR studies:

1. Approximately 25 patients per year will be studied using fast spectroscopic imaging without contrast agents. FSI will be correlated quantitatively with conventional MRI and biopsy.

2. Approximately 25 patients per year will be given contrast. Time resolved FSI images of contrast uptake will be analyzed to measure rates of contrast uptake and accurately identify the boundaries of enhancing regions. T_1-weighted and T_2*-weighted images of contrast agent uptake will be synthesized. **FSI** images will be correlated quantitatively with conventional MRI and biopsy

3. Quantitive analysis of FSI data and quantitative comparison with conventional images: We will extend previous work of Drs. Guilhuijs and Giger to provide quantitative analysis of **FSI** and conventional images. We will compare edge sharpness, texture, temporal and spatial gradients in contrast media uptake, signal-to-noise ratio, and contrast-to-noise ratio in FSI and conventional MR images.

E. MR data will be correlated with biopsy, conventional MR images, and mammography.

(3) **BODY:**

During the previous budget year we made significant progress towards achieving the specific aims of the proposal. We have:

1. Implemented FSI methods on our GE SIGNA 1.5 Tesla scanner.
2. Tested the methods in phantoms and also in human brain (see below).
3. Continued development of methods for processing the data (see below).

4. Initiated studies of patients who are being treated for breast cancer and women who are at increased risk for breast cancer because of family history, genotype, and/or a previous history of cancer.

We have made two changes in our plans for this research. Because of the complexity of development of HiSS imaging for breast we have done some work in two model systems to guide our methods developments:

1) In addition to the scans of phantoms that were planned, we have performed additional HiSS imaging of human brain. The rationale for this is that brain anatomy is well defined so that we can judge whether our pulse sequences are giving us accurate anatomic information.

2) We have performed some HiSS imaging in rodent tumor models to develop methods for processing and analyzing HiSS data to differentiate between metastatic and non-metastatic cancer.

The costs of scans of human volunteers and rodent tumor models are not charged to this grant - the scans are simply added on to experiments that are funded by other means. The data acquired are used as a test bed for developing methods that are being used for scans of breast.

Details of our progress in some of these areas are given below:

SOW A and C: Clinical HiSS has been implemented on the SIGNA whole body scanner with reasonable run-times. We have implemented high spectral and spatial resolution imaging on one of our SIGNA 1.5 Tesla whole body scanners. The pulse sequence – an echo planar spectroscopic imaging sequence - allows acquisition of 128 - 256 gradient echoes with echo spacing between 2.5 msec and 8 msec – and echo train length of between 300 msec and 750 msec. This means that spectral resolution can be as high as 1.2 Hz and spectral bandwidth can be as high as 400 Hz. Spatial matrix size is 256 by 256 so that high spatial resolution can be obtained. As an initial test of image quality, we have performed scans of brain, since brain anatomy is well defined and thus image accuracy and quality can easily be evaluated.

Figure 1

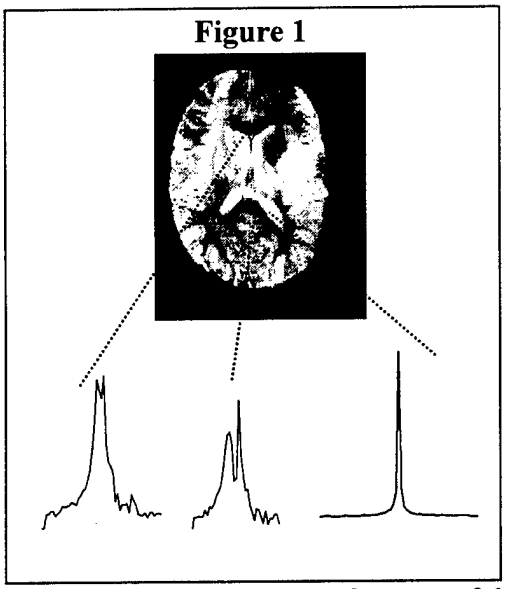

HiSS images of brain in which image intensity is proportional to water signal peak height show excellent contrast and edge delinieation. In-plane resolution was 750 microns in a 4 mm thick slice, with spectral resolution of 1.2 Hz. The images are similar to proton density images but have much higher contrast between white and gray matter and shows details not generally detected in conventional images. High resolution water resonances associated with several voxels are also shown. The dashed lines indicate the relationship of anatomical regions to specific spectra. Note that two of the water resonances are inhomogeneously broadened and contain two or more resolved components. The resonance from the voxel in the cerebral spinal fluid is a narrow lorentzian - **suggesting that eddy current effects are small**. Various features of the water signal lineshape were used to synthesize images (i.e. height of shoulder, number of shoulders, peak asymmetry). The effects of contrast agents on the resolved components can be measured. We will continue to optimize pulse sequences in the clinical scanner so that we can apply HiSS imaging to beast cancer.

SOW B. We are developing methods for processing HiSS (High Spectral and Spatial Resolution) MRI data from tumors (see manuscript submitted to Journal of Magnetic Resonance in Medicine in Appendix). Some of the preliminary work is being done in rodent tumors to improve flexibility and reduce data collection costs. We have found that HiSS differentiates between non-metastatic and metastatic tumors based on contrast media uptake and image texture. A preliminary study of rodent Dunning prostate tumors is underway to test the use of HiSS MRI as a means of differentiating non-metastatic and metastatic rodent prostate tumors based on quantitative measurements of image texture and contrast enhancement. Edge enhanced images of metastatic tumors are more heterogeneous than those of non-metastatic tumors. Image texture, S_r is significantly larger for the metastatic tumors (average S_r value 5.9 ± 2.6 arbitrary units) than the non-metastatic tumors (average S_r value 3.0±1.1), i.e., the surface variations in image intensity are much greater in metastatic tumors ($p < .0005$ by T-test before contrast injection, and $p<.0001$ after contrast injection). These data demonstrate the sensitivity of HiSS to the textural complexity of tumors. Combining various measurements of texture in contrast enhanced images with measures of contrast media uptake as an indicator of blood volume improved the separation between metastatic and non-metastatic tumors. A manuscript describing this work has been submitted to Magnetic Resonance in Medicine. This exercise is yielding important results, and is helping us to develop data acquisition and analysis methods which can be used to process clinical data.

SOW D. Breast scans of healthy volunteers, women with suspicious breast lesions, and women who are being treated for breast cancer: We have performed 6 HiSS scans of healthy volunteers and 5 of women with suspicious breast lesions. The HiSS images are compared with fat suppressed and T1 and T2 weighted fast spin echo images. A typical HiSS image (peak height of the water proton spectrum) is shown below. HiSS images appear to show substantially different contrast than conventional MR images and to have some advantages for detection of breast lesions. However, the amount of data accumulated to date is too small to allow rigorous statistical analysis.

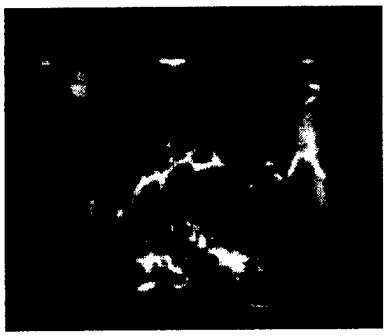

Figure 2

SOW D. Dynamic contrast enhanced scans of patients with breast cancer have been obtained. We have begun preliminary studies of patients with prostate cancer metastatic to the bone. Omniscan is injected I.V. and uptake in a selected region containing a single metastasis or multiple metastases is followed. Currently we are performing fast spoiled gradient recalled echo imaging with restricted spatial resolution and image volume to obtain high temporal resolution immediately before and after injection of the contrast agent so that the first pass of the bolus can be accurately detected. Figure 3 shows a typical data set. Images obtained before and after

contrast injection are shown and a plot of contrast agent vs. time is shown. A strongly and rapidly enhancing lesions is clearly visible. Although we are not yet using the fast HiSS sequences to detect contrast media uptake, these preliminary studies establish a mechanism for recruiting and scanning patients and provide an estimate of the sensitivity of contrast enhanced MRI.

Figure 3

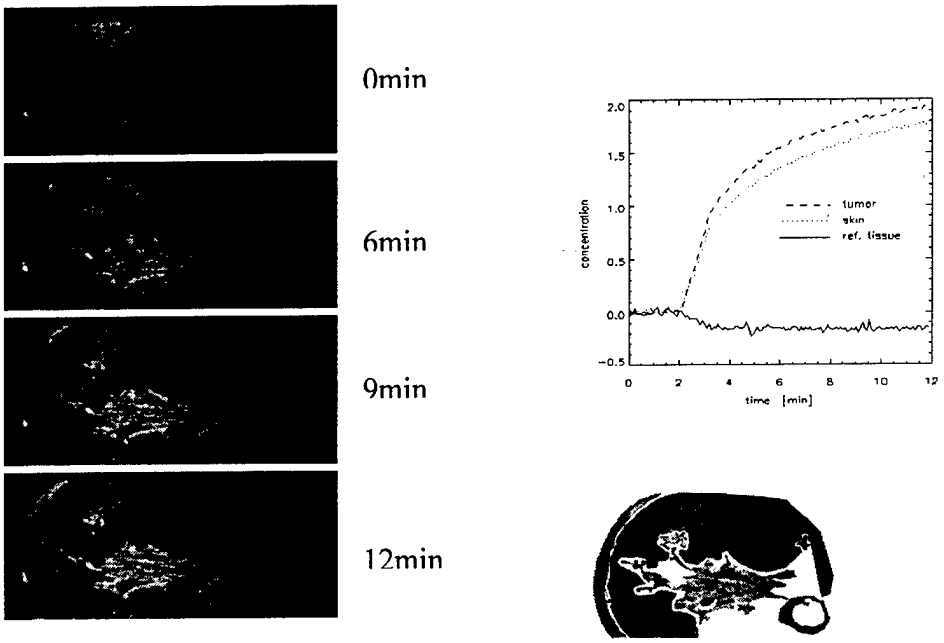

(4) **KEY RESEARCH ACCOMPLISHMENTS:** *Bulleted list of **key** research accomplishments emanating from this research*

- Implementation of fast HiSS MR imaging methods based on EPSI on clinical scanners.
- Development of methods based on HiSS to differentiate non-metastatic and metastatic tumors.
- Tests of anatomic accuracy of HiSS in brains of normal volunteers.
- HiSS scans of breast of healthy volunteers, women with suspicious breast lesions, and women who are being treated for breast cancer.

(5) **REPORTABLE OUTCOMES::**

– manuscripts, abstracts, presentations;

1. **GS Karczmar,** X Fan, H Al-Hallaq, JN River, K Tarlo, K Kellar, M Zamora, C Rinker-Schaeffer, and Martin J Lipton. Functional and Anatomic Imaging of Tumor Vasculature: High Resolution MR Spectroscopic Imaging Combined with a Superparamagnetic Contrast Agent. Academic Radiology, in press.

2. **GS Karczmar**, X Fan, JN River, H Al-Hallaq, M Zamora, C Rinker-Schaeffer, P Losco, K Tarlo, K Kellar. Uptake of a superparamagnetic contrast agent imaged by MR with high spectral and spatial resolution. Magnetic Resonance in Medicine **43:** 633-639, 2000.

3. H Al- Hallaq, M Zamora, BL Fish, JE Moulder, **GS Karczmar**. MRI measurements correctly predict the relative effect of tumor oxygenating agents on hypoxic fraction in rodent BA1112 tumors. International Journal of Radiation Oncology, Biology, and Biophysics, **47:** 481-488, 2000.

4. J. Evelhoch, **G Karczmar**, J Koutcher, R Maxwell, Orhan Nalcioglu, Natarajan Raghunand, B Ross, H Swartz. Applications of Magnetic Resonance in Model Systems: II. Cancer Therapeutics". Neoplasia, in press.

Submitted Papers:

1. X Fan, H Al-Hallaq, JN River, M Zamora, K Tarlo, K Kellar, C Rinker-Schaeffer, MM Zaucha, and **GS Karczmar**. Improved Contrast and Resolution: Calculation of Pure Absorption Images from High Spectral and Spatial Resolution MR Data. Medical Physics

2. HA Al-Hallaq, MZ Zamora, BL Fish, JE Moulder, H Halpern, and **GS Karczmar**. MRI Measurements correctly predict the relative effects of tumor oxygenating agents in rodent BA1112 tumors. Proceedings of the International Society on Oxygen Transport to Tissue, 2000.

4. HA Al-Hallaq, M Zamora, JE Moulder, **GS Karczmar.** Measurement of spectrally inhomogeneous BOLD contrast changes in rodent tumors by high spectral and spatial resolution (HiSS) MRI. Magnetic Resonance in Medicine, submitted.

– patents and licenses applied for and/or issued;

– degrees obtained that are supported by this award;

Al-Hallaq- Ph.D . awarded July, 2000

Weiliang Du, PhD. Expected 2002

– funding applied for based on work supported by this award;

We are currently applying for an NIH R21 which will allow extension of this work to studies of rodent tumor models.

CONCLUSIONS: The progress to date suggests that HiSS can be successfully implemented on clinical scanners and produce high quality images which contain information that is not available in conventional MR scans. HiSS MRI is particularly useful for detection of contrast agents. It is likely that HiSS will produce a significant increase in sensitivity and specificity of MRI for detection of breast cancer as well as other cancers. This means that cancers can be detected early

when they are highly treatable. Earlier cancer detection is likely to improve clinical outcome for many cancer patients.

During the next year of support we plan to continue to optimize HiSS MRI on the clinical scanner. At the same time, we will begin to scan patients with breast cancer to determine whether HiSS MRI provides significant increases in the sensitivity and accuracy of cancer detection and staging. We believe that based on the difficulty of optimizing HiSS data acquistion and analysis on clinical scanners, a limited amount of work using animal model tumors as a 'test bed' continues to be justified.

(6) APPENDICES: Fan et al.

Differentiation of Non-Metastatic and Metastatic Rodent Prostate Tumors with High Spectral and Spatial Resolution MRI

Xiaobing Fan[1], Jonathan N. River[1], Marta Zamora[1], Kirk Tarlo[3], Kenneth Kellar[3], Carrie Rinker-Schaeffer[2], and Gregory S. Karczmar[1+]

Departments of [1]Radiology and [2]Urology
University of Chicago
Chicago, IL 60637

and

[3]Nycomed Amersham
Princeton, NJ 08540

SUBMITTED TO: **Magnetic Resonance Medicine (MRM-100-4799)**

[+]Address Correspondence To:

Gregory Karczmar, Ph.D.
Associate Professor
Department of Radiology, MC2026
University of Chicago
5841 S. Maryland Ave.
Chicago, IL, USA 60637

Phone: 773-702-0214
Fax: 773-702-1161
Email: gskarczm@midway.uchicago.edu

ABSTRACT

MR images can be acquired with high spectral and spatial resolution to precisely measure lineshapes of the water and fat resonances in each image voxel. Previous work suggests that the high resolution spectral information can be used to improve image contrast, signal-to-noise ratio, sensitivity to contrast agents and to physiologic and biochemical processes that affect local magnetic susceptibility gradients. The potential advantages of high resolution spectroscopic imaging (SI) suggest that it might be useful for early detection and characterization of tumors. The present experiments evaluate use of high resolution SI to discriminate between metastatic and non-metastatic rodent Dunning prostate tumors. SI datasets were obtained at 4.7 Tesla with in-plane resolution of 350-500 microns in a single 1.0 mm slice, and 6-8 Hz spectral resolution, before and after I.V. injection of an iron oxide contrast agent. Images of water signal peak height in non-metastatic tumors were smoother in the tumor interior than images of metastatic tumors ($p < .004$ by T-test) before contrast media injection. This difference was stronger in contrast enhanced images ($p < .0004$). In addition, the boundary between the tumor and muscle was more clearly demarcated in non-metastatic than metastatic tumors. Combinations of image texture, tumor edge morphology, and changes in T_2^* following contrast media injection improved discrimination between metastatic and non-metastatic tumors. The data presented here do not demonstrate that effective discrimination between metastatic and non-metastatic tumors depends on the use of high resolution SI. However, the results suggest that SI and/or other MR methods that provide similar contrast might be used clinically for early and accurate detection of metastatic disease.

INTRODUCTION

Sensitive and accurate non-invasive imaging methods are needed to detect breast and prostate cancer at an early stage and accurately identify metastatic disease. Screening measures such as blood tests for prostate-specific antigen have been useful for targeting groups with histological prostate disease. However only twenty percent of American men above the age of 50 with histological evidence of disease have clinically important disease, i.e., disease that may metastasize and result in death [1,2]. Similar considerations apply to breast cancer; breast lesions must be detected early and since the majority of suspicious lesions found by screening procedures are not dangerous, it is important to distinguish between those with high metastatic potential and those with little or no malignant potential [3]. MRI is a strong candidate for detection and evaluation of breast and prostate abnormalities because it has strong soft tissue contrast and is non-invasive. In addition, intravascular MR contrast agents can be used to detect high blood flow, vascular density, and capillary permeability that often characterizes metastatic lesions (e.g. [4-7]). However, despite a great deal of effort MRI studies of prostate cancer and breast cancer patients have not conclusively demonstrated the high sensitivity and specificity that would justify routine clinical use of this approach.

Improved approaches to data acquisition and analysis are needed to increase the sensitivity and specificity of MRI. Here we evaluate the potential of high spectral and spatial resolution MR imaging to improve detection and classification of suspicious lesions. High resolution spectroscopic imaging (referred to in the following as high resolution SI, or SI) is a natural extension of the pioneering work of Dixon et al. [8] and Glover et al. [9], demonstrating that spectral information at low resolution can greatly improve image quality by separating water and fat signals and correcting images for B_0 field inhomogeneities. More recently, images have

been acquired with increased spectral resolution to resolve the details of the water (and fat) lineshape in each image voxel [10-13]. For example we have obtained images with high spatial resolution and spectral resolution as high as 3 Hz at 4.7 Tesla [11,12,14-16]. The rationale for high resolution SI is that the water signal from living tissue is generally homogeneously broadened and often contains multiple resolvable components [14,16,17] due to local, sometimes microscopic magnetic susceptibility gradients. These gradients reflect local anatomy and physiology, as well as the effects of synthetic contrast agents [16,17]. The shape of the water resonance can be an important source of image contrast – for example, images can be synthesized with intensity proportional to the amplitude, resonance frequency, integral, and linewidth of the entire envelope of the water signal or of its individual components. Other features can also be used to produce images, e.g. the number of components in the water signal or the asymmetry of the water envelope. High resolution SI produces images with stronger T_2^* contrast than is available in conventional gradient echo images because the proton signal can be followed for many hundreds of milliseconds, without the destructive interference between the various Fourier components of the water resonance that degrades gradient echo images at long TE. Work from several laboratories has suggested potential advantages of high resolution SI, including improved signal-to-noise ratio, image contrast, edge delineation, and increased sensitivity to contrast agents [10-14,18]. High resolution SI has also been used to improve detection of changes in local tumor blood oxygenation caused by tumor oxygenating therapies [11,14]. SI is particularly useful in tumors, where the proton signals *in vivo* are often complex due to deoxygenated blood, hemorrhage, sequestration of iron, and a generally inhomogeneous microenvironment [14,16,17].

The potential advantages of high resolution SI suggest that it may facilitate sensitive and accurate detection of cancer by MR. The purpose of the present work is to evaluate whether or not contrast-enhanced high resolution SI reliably discriminates between metastatic and non-metastatic cancer in a well defined, stable rodent tumor model. In the experiments reported here we used high resolution SI to image Dunning AT2.1 (non-metastatic) and AT3.1 (metastatic) prostate tumors implanted in the hind limbs of Copenhagen rats. We compared image texture, tumor boundaries, and effects of a superparamagnetic iron oxide contrast agent in the two cell lines.

METHODS

Tumors

Experimental protocols involving animals were approved by the University of Chicago Animal Care and Use Committee (Protocol # 70784R) and were consistent with federal, state, and local regulations. Metastatic (Dunning AT3.1) and non-metastatic (Dunning AT2.1) tumors were grown in the hind limbs of Copenhagen rats. R3327 prostatic cancer cell lines AT2.1 (n=8) (low metastatic potential) and AT3.1 (n=7) (high metastatic potential) [19,20] were grown in standard RPMI-1640 medium (Cellgro, Mediatech/CellGro, Herndon, VA) containing 8% fetal calf serum (Gibco-BRL, Inc.), penicillin (10,000u), streptomycin (100 ug/ml; Gibco-BRL, Inc.), and 250 nM dexamethasone (Sigma Chemical Co., St. Louis, MO). The tumor cells were subcutaneously injected (2×10^5 cells per injection) into rat hind limbs using a 26 G needle. Rats were anesthetized with isofluorane during the injection.

Contrast agent

NC100150 (Clariscan^{TM}, Nycomed-Amersham, Princeton, New Jersey and Amersham, UK) was injected I.V. at a dose of 2 mgs/kg. NC100150 is a superparamagnetic particulate, currently in phase III clinical trials, with average diameter (including iron core and oxidized starch coating) of 15 – 20 nanometers, R_1 of 8 $mM^{-1} * sec^{-1}$, and R_2 of ~40 $mM^{-1}*sec^{-1}$ at 4.7 Tesla (21). The contrast agent had no measurable effects on animals' blood pressure, heart rate or temperature.

Anesthesia, immobilization, and monitoring of rats during MR experiments

On the day ~~of~~ the MR experiment, anesthesia was initially induced with isofluorane, and a ketamine hydrochloride (90 mg/kg) - xylazine (10 mg/kg) mixture was then injected I.P. A catheter (PE 50 tubing) was inserted into the external jugular vein for injection of the contrast agent. During MR measurements, animals were anesthetized by continuous I.P. administration of ketamine (90 mg/kg per hr) and rompun (5 mg/kg per hr). The temperature of the animals was controlled using a warm water blanket, and in addition the magnet was continuously flushed with warm air using an animal cage dryer. To minimize motion artifacts, rats were secured to a Plexiglas board using vet wrap and tape. The tumor bearing leg was immobilized horizontally, placed in the Helmholtz detector coil and secured with tape. The long axis of the leg was placed perpendicular to the main magnetic field. A capillary tube filled with water was placed inside the coil above the tumor and was used as a marker for the midline of the tumor in MR images. Blood pressure was continuously measured during MR studies using a catheter (PE-50) implanted in the femoral artery attached to a pressure transducer and a Tektronix monitor. Animal temperature was continuously measured using a rectal thermometer (Fisher Scientific, Springfield, N.J.). Approximately 60 minutes were required to prepare and position the animal in the magnet.

MR measurements

MR experiments were performed using a 4.7 Tesla GE/Bruker Omega scanner (Fremont, CA) equipped with self-shielded gradient coils. A Helmholtz coil was used for signal excitation and detection. The high resolution spectroscopic images were obtained using the approach developed by Brown *et al.* (22) and Maudsley *et al.* (23); following slice selection, phase encoding gradient pulses were applied along two axes before detection of the proton free induction decay to provide spatial resolution. A single 1.0 mm thick slice through the center of the tumor was imaged with in-plane resolution of 350-500 microns (64×64 points) and frequency resolution of 6.0 - 8.0 Hz. The total acquisition time for each spectroscopic image was 11 - 14 minutes. Sequential images were collected before and after injection of contrast agent.

Calculations of peak height and T_2^*-weighted images from absorption spectra

Water and fat spectra were corrected for truncation artifacts and the pure absorption spectra in each pixel were calculated using the method described by Fan *et al.* (24). Images were calculated with intensity proportional to water signal peak height and T_2^*. With complex spectra such as those found in tumors (14,16,17) T_2^* (or linewidth) is not well defined, but approximately T_2^*-weighted images were calculated from absorption spectra by measuring the inverse line width of the water signal at the half peak height. An additional empirical estimate of the linewidth was obtained by dividing the integral by the peak height of each resonance. Other parameters derived from water signal lineshape might enhance discrimination between metastatic and non-metastatic tumors. However, water signal peak height and linewidth can be determined with high signal-to-noise ratio and are sensitive to all of the Fourier components that contribute to the water resonance.

Quantitative measures of image texture and edge delineation

To determine image texture, image intensity (z) was defined as a function (f) of the x and y locations of each pixel:

$$z = f(x, y). \tag{1}$$

The surface area of the function (z) was found numerically from the following equation,

$$S = \sum \sqrt{1 + f_x^2 + f_y^2}, \tag{2}$$

where the summation is over the region of interest (e.g. the tumor), $f_x = \partial f / \partial x$, and $f_y = \partial f / \partial y$.

The function $\sqrt{1 + f_x^2 + f_y^2}$ exhibits maxima at the pixels where the derivatives of peak intensity with respect to spatial coordinates x and y are larger, for example, at the edge of the tumor. Therefore, this function could be used to display images that emphasize the variations of peak intensity. As a measure of the texture of the image, we defined the parameter 'S_r',

$$S_r = 100.0 \cdot \left| S(\text{tumor}) - S_{xy} \right| / S_{xy}, \tag{3}$$

where S(tumor) is the surface area of the function, 'z' (arbitrary units), in the region of interest calculated from Equation 2, and S_{xy} is the projection of S(tumor) onto the x-y plane. S_r measures the variation in image intensity over the projected area. If image intensity in the region of interest is constant, S_r is 0, whereas highly variable image intensity results in a large S_r. To minimize noise the peak height images (which have high signal-to-noise ratio and contrast) were used in the analysis. Since gain and other instrumental parameters were different for each experiment, the S_r value directly calculated from the peak height image could not be compared between experiments. Therefore the intensity of peak height images was normalized by dividing by the average intensity in the muscle region for each experiment prior to

calculating S_r. Edge enhanced images were calculated from the peak height images by using the formula in Equation 2 without summation.

The ratio (I_r) of average image intensity in the tumor to average intensity in the muscle was defined as

$$I_r = I_{\text{average}}(\text{tumor}) / I_{\text{average}}(\text{muscle}), \tag{4}$$

where $I_{\text{average}}(\text{tumor})$ is the average intensity of a region in the tumor, and $I_{\text{average}}(\text{muscle})$ is the average intensity in the selected muscle region. Since muscle was assumed to be the same in both non-metastatic and metastatic tumors, I_r is a normalized measure of average intensity in the tumors.

As a measure of the irregularity of the tumor border, we calculated the ratio (A_r) of the tumor area to that of a circle that has the same circumference as the tumor,

$$A_r = A_c / A_{ROI}, \tag{5}$$

where A_{ROI} is the tumor area with the boundary traced manually with IDL software (Research Systems, Inc., Boulder, CO), and A_C is the area of the corresponding circle. Thus, A_r is large if the tumor boundary is irregular, and close to 1 if the tumor boundary is smooth.

Contrast agent kinetics

The average T_2^* of the water resonance in the tumor reached a minimum immediately after NC100150 contrast agent injection. We calculated the maximum decrease in T_2^* or increase in $1/T_2^*$ (R_2^*) averaged over the entire tumor – using only those pixels in which T_2^* decreased. Changes in R_2^* (ΔR_2^*) are approximately proportional to the concentration of contrast agent in each voxel. Since the contrast agent is intravascular at early times after injection ΔR_2^* is sensitive to tumor blood volume. This is only a qualitative measure of tumor blood volume

because of leakage of the contrast media into the extravascular space and the fact that the low time resolution of the data did not permit extrapolation of ΔR_2^* to time '0'. Rapid diffusion-mediated exchange of magnetization between the intravascular and extravascular spaces (25) may also have reduced the accuracy of blood volume measurements.

Contrast media washout rate was measured based on the rate at which R_2^* returned to the control value following the maximum increase (i.e. decrease in T_2^*). The concentration of NC100150 as a function of time, $C(t)$, generally reached a maximum in the first image obtained after injection (t ~ 10 minutes after injection) and then decayed monotonically toward '0'. $C(t)$ was modeled as an exponential decay curve starting where $C(t) = C_{max}$.

Synthesis of gradient echo images

The purpose of the present work was to evaluate the use of high resolution SI to discriminate between metastatic and non-metastatic tumors. Statistically meaningful comparison of high resolution SI with conventional imaging is not supported by the present results. However, to obtain a crude qualitative comparison of SI with gradient echo imaging, gradient echo images were synthesized from SI datasets. To do this, points on each phase encoded proton free induction decay acquired between ~20 msec and ~25 msec after excitation were summed and a 2DFT with respect to the phase encoding gradient amplitude was used to obtain images. This simulates gradient echo images acquired with TE/TR of approximately 20 msec/140 msec and a bandwidth of ~12 kHz. The images were then analyzed to determine measures of texture as described above.

RESULTS

Fig. 1 and Fig. 2 show all control peak height images (A), edge enhanced images (B), and difference images (C) (immediately after contrast injection minus before injection) for non-metastatic and metastatic tumors, respectively. The images are displayed in the order the experiments were performed from the most recent '1' to earliest '12'. The orientations of the imaging slices are sagital, i.e. perpendicular to the long axis of the legs, except that image 12 in Fig. 1, and images 6, 8, and 12 in Fig. 2 are axial. (Note that the long axis of the leg is perpendicular to main field.) A summary of estimated tumor growth rates and tumor cross-sectional areas (determined from images) is given in Table 1. The numbers in column '1' correspond to the image numbers in Figs. 1 and 2. The average tumor growth rate and cross-sectional area are less in non-metastatic tumors (0.07 ± 0.02 cm^3/day and 0.85 ± 0.14 cm^2, respectively) compared to metastatic tumors (0.11 ± 0.02 cm^3/day and 1.20 ± 0.16 cm^2, respectively (mean ± standard error)). However, these differences are not significantly different. Size and growth rate did not correlate with any of the MR parameters measured.

Regions of interest for the interior of each tumor and for the entire tumor (i.e. excluding and including the edge of the tumor, respectively) were traced manually from the edge enhanced images. Equation 3 was then used to calculate S_r(tumor interior) and S_r(entire tumor) from images obtained immediately before contrast media injection and at the time after contrast media injection when ΔR_2^* was largest. These parameters are listed for each tumor studied in Table 1. Various combinations of parameters were used to generate 2-dimensional plots to improve separation of metastatic and non-metastatic tumors. Fig. 3 shows S_r(tumor interior, before contrast agent injection; S_r is given in arbitrary units) for all 24 tumors plotted against the values of S_r obtained after contrast injection. Before contrast agent injection S_r(interior) was significantly larger in the metastatic tumors than the non-metastatic tumors (see Table 2), i.e., the

surface variations are much greater in metastatic tumors ($p < 0.004$ by two-tailed T-test). After contrast agent injection the separation between the distributions of metastatic and non-metastatic tumors improved to $p < 0.0004$. Although the differences between metastatic and non-metastatic tumors were highly statistical significant, classification of individual metastatic and non-metastatic tumors based on S_r was not completely reliable. Fig. 3 demonstrates significant overlap between the two distributions.

The edge enhanced images suggest that the non-metastatic tumors generally have a more clearly demarcated boundary between the tumor and muscle/skin than the metastatic tumors. At the present spatial resolution, edges were difficult to define precisely, but an approximate measure of the sharpness of tumor edges was obtained by subtracting S_r(interior) from S_r(entire tumor) (see Table 2) to give approximately $\sim S_r$(tumor rim). $\sim S_r$(tumor rim) was significantly larger in non-metastatic tumors (2.6 ± 0.5) than in metastatic tumors (0.8 ± 0.3; $p<.007$ by T-test) before contrast injection. A two dimensional plot of S_r(interior) with contrast agent vs. $\sim S_r$(tumor rim) without contrast agent (Figure 4) gives excellent separation between non-metastatic and metastatic tumors - only one non-metastatic tumor falls within the distribution of metastatic tumors.

The average of maximum T_2^* changes before and just after injection of contrast in the tumor and selected muscle regions were calculated and are listed in Table 1 for all the experiments. These changes were calculated based only on those pixels in which T_2^* decreased (see below) in an attempt to emphasize those regions with very high vascular density. Fig. 5 shows the S_r(interior) values just after injection of contrast agent as a function of average maximum T_2^* changes. The average maximum T_2^* changes in non-metastatic tumors were higher (see Table 2) and more spatially uniform than those in metastatic tumors. Therefore the combination of maximum T_2^* changes and S_r measurements tends to separate the metastatic and

non-metastatic tumors (Fig. 5), although there is some overlap between the distributions. Contrast media washout rates were not significantly different in non-metastatic and metastatic tumors and combinations of washout kinetics and various texture parameters did not help to separate the two populations.

The values for 'S_{rdiff}' were also calculated for difference images, i.e. water signal peak height in the first image after contrast injection minus control peak height. These S_{rdiff} values do not clearly distinguish metastatic and non-metastatic tumors because of the very large range of values for metastatic tumors (Table 2). The I_r values (average intensity relative to muscle) and the changes in I_r after contrast media injection do not effectively discriminate between metastatic and non-metastatic tumors. The difference in average values of A_r (irregularity of tumor border) between the metastatic and non-metastatic tumors is also very small (Table 2). Tumor growth rate and tumor size did not correlate well with any of the measures of image texture, tumor architecture, or contrast media dynamics (see Table 1).

The response to the contrast agent within the tumors (but not in muscle) is heterogeneous both among pixels and among spectral components within each voxel [16,17]; there are both increases and decreases in water signal peak height. Analysis of the linewidth of the water resonance in each voxel demonstrates that these early changes are due primarily to changes in linewidth (T_2^*) rather than changes in the water signal integral.

In metastatic tumors during the first ~10 minutes after contrast media injection T_2^* decreased in 65% of voxels and increased in 35%. In the voxels with decreased T_2^* the average decrease was 3.2 ± 0.4 msec while in the voxels with increased T_2^* the average increase was 2.3 ± 0.4 msec (errors are standard error of the mean). In non-metastatic tumors T_2^* decreased in 76% of voxels and increased in 24%. The average decrease was 4.8 ± 0.9 msec and the average

increase was 1.4 ± 0.3 msec. Thus, decreases in T_2^* or increases in water signal linewidth were predominant, but more so in non-metastatic tumors than in metastatic tumors.

Gradient echo images synthesized from SI datasets also distinguished between metastatic and non-metastatic tumors based on the image texture. S_r derived from the synthesized gradient echo images was greater in the interior of metastatic tumors than in the interiors of non-metastatic tumors. The difference was statistically significant at the $p < 0.06$ level without contrast agent, and at the $p < 0.02$ with contrast agent.

DISCUSSION

Surface areas of 3D representations of tumor images (intensity versus xy position) were used as a measure of image texture. The texture of tumor interiors (S_r or S_{rdiff}) was significantly 'rougher' in metastatic tumors than in non-metastatic tumors. Differentiation between metastatic and non-metastatic tumors based on texture improved greatly after I.V. injection of the contrast agent. The regions of largest S_r tended to coincide with the regions where decreases in T_2^* were largest following contrast media injection. As a result, the contrast agent accentuated S_r, perhaps because regions with high S_r are regions with dense vasculature where the intravascular contrast agent causes large susceptibility gradients. A combination of image texture analysis (S_r after contrast) and blood volume measurement (maximum change in T_2^* after contrast injection) was also effective in distinguishing metastatic and non-metastatic tumors.

Tumor edges were more clearly defined in non-metastatic than in metastatic tumors. The differences were difficult to define precisely because at the present spatial resolution, tumor rims could not be accurately segmented. Nevertheless the approximate values calculated for S_r(tumor rim) combined in a 2-dimensional plot with S_r(interior) gave excellent separation between

metastatic and non-metastatic tumors. The rather poorly defined edges of metastatic tumors suggest effects of the metastatic tumors on surrounding tissue – perhaps due to infiltration. The very clear separation between the two tumor populations reported here, particularly in Fig. 4, is based on studies of a small number of tumors (12 metastatic and 12 non-metastatic). The sensitivity and specificity implied by the current results may not persist when much larger numbers of tumors are imaged. Nevertheless, the results are encouraging and suggest that a combination of texture and hemodynamic measurements obtained from contrast enhanced high resolution SI may provide optimal separation of metastatic and non-metastatic tumors.

NC100150 had spatially and spectrally heterogeneous effects on T_2^*. Although decreases in T_2^* were predominant, there were significant increases in T_2^* in some tumor regions. The prevalence and magnitude of T_2^* increases were greater on average in metastatic than in non-metastatic tumors. There are a number of potential explanations for this effect. NC100150 at the correct concentration can decrease water signal line width by matching magnetic susceptibility between two adjacent regions (26). This is most likely to occur in regions with large veins or dense vasculature with high deoxyhemoglobin levels where plasma NC100150 matches the magnetic susceptibility due to deoxyhemoglobin inside the red blood cells – or where intravascular NC100150 matches high extravascular magnetic susceptibility due to extravasated hemoglobin. Alternatively, apparent changes in T_2^* can occur if the T_1 of a narrow component of an inhomogeneously broadened water resonance is increased relative to other components of the resonance (11). Further investigation is needed to properly characterize this phenomenon.

Although we found highly statistically significant differences between metastatic and non-metastatic tumors, there was significant overlap between the two distributions. If similar methods were used in a clinical setting, many metastatic tumors could be reliably identified, but some metastatic tumors would be missed since they fall within or close to the non-metastatic

distribution. This degree of overlap between uniform, stable, highly metastatic and non-metastatic rodent tumors calls into question whether clinical MRI, as currently practiced, can distinguish between malignant and benign lesions in a highly variable population of human patients. Although rodent tumors are far from perfect models for human disease, they share fundamental characteristics of human tumors, e.g., metastatic tumors in both species have regions of high angiogenic activity, rapid and irregular growth, and invasion of surrounding tissue [19,20]. Thus, the present results obtained with rodent tumors are relevant to human disease. As in the case of the present results, hemodynamic and/or textural analysis in studies of breast lesions in patients often yields a relatively narrow distribution for benign lesions, and a broad distribution for metastatic lesions [27]. More work is necessary to increase understanding of why some metastatic tumors fall within the normal tumor distribution and some do not – and what data acquisition and analysis methods should be used to increase our power to resolve the two populations of tumors.

We anticipate that there are several ways in which the sensitivity and specificity of high resolution SI could be increased :

1. The sensitivity and specificity of high resolution SI might increase if measurements of image texture and blood volume excluded necrotic and dormant tumor regions since these regions are not actively metastatic. Many of the tumors shown in Figs. 1 & 2 clearly contain such regions, e.g., regions that do not take up the contrast agent. These regions tend to have relatively low values of the texture parameter, S_r. For example, image intensity does not change greatly following contrast media injection in large portions of non-metastatic tumors 4 and 6 and metastatic tumors 4, 6, and 12 and the images are fairly smooth in these regions. Such regions could, in principle, be automatically identified based on response to contrast media but the spatial resolution of the images in the current datasets does not allow accurate segmentation.

Spatial resolution can be increased through the use of much faster spectroscopic imaging methods (see below).

2. The sensitivity and specificity of high resolution SI might also be improved through use of additional features of the water signal lineshape. The results presented here are based on water signal peak height in each voxel. Peak height is sensitive to relatively subtle changes in water signal lineshape, since it is determined by the combined contributions of all the Fourier components of the water signal. However, other features of the water resonance might provide improved discrimination between metastatic and non-metastatic tumors. For example, images could be synthesized from the amplitudes, linewidths, or resonance frequencies of individual components of the water signal, asymmetry of various components, or higher moments of the water resonance.

3. Further improvement could come through imaging multiple slices through tumors. Due to the time required for acquisition of phase encoded spectroscopic images, only single slice in each tumor was imaged. This could lead to sampling artifacts, i.e. the imaged slice may not always have accurately represented the entire tumor. In the future, fast imaging with higher spatial resolution over larger volumes (obtained using echo planar spectroscopic imaging methods, see below) will allow more detailed examination of the whole tumor.

4. Improved sensitivity and specificity of dynamic, contrast enhanced SI after injection of contrast agent might be achieved using fast spectroscopic imaging methods (also known as echo planar spectroscopic imaging [28-30]). This approach provides SI datasets with much higher temporal, spatial, and spectral resolution [12,13] than that achieved with the conventional phase encoding method used here. Thus, temporal resolution could be increased during the early phase of contrast media uptake. During the later phase of contrast media distribution, larger volumes of tissue could be imaged with higher spatial resolution. This is achieved at the cost of some

decrease in signal-to-noise ratio (12). However the SI datasets do not appear to be signal-to-noise ratio limited, and work in this laboratory (12) and other laboratories (10,13) demonstrates that fast spectroscopic imaging provides high quality MR images.

The purpose of the present experiments was to evaluate the utility of high resolution SI for accurate classification of metastatic v.s. non-metastatic tumors, rather than to compare SI with conventional MRI methods. Therefore the question of whether SI distinguishes metastatic and non-metastatic tumors more reliably than conventional MRI was not directly addressed by the present experiments. The very qualitative comparison of gradient echo imaging and SI reported here suggests that both approaches can distinguish between metastatic and non-metastatic tumors based on textural parameters - but that SI identifies metastatic tumors with a higher level of confidence. However, the synthetic gradient echo images did not have optimal signal-to-noise ratio, and both the gradient echo and spectroscopic images had sub-optimal spatial and temporal resolution. Work is currently underway to thoroughly compare the two approaches under optimal conditions and to determine whether the putative advantages of high resolution SI are in part responsible for the strong statistical differences between metastatic and non-metastatic tumors reported here.

CONCLUSIONS

The results of the present study of rodent prostate tumors suggest that contrast enhanced high resolution spectroscopic imaging can discriminate between metastatic and non-metastatic tumors based on measures of image texture, tumor edges, and contrast agent dynamics. SI may be particular useful in this context because the water resonance in tumors is often complex and

has multiple resolvable components – and because effects of superparamagnetic contrast agents are likely to be spectrally heterogeneous (16,17).

ACKNOWLEDGEMENTS

Support for this work was provided by the American Cancer Society (CCE-86272), the National Cancer Institute (1RO1CA76476 & 1RO1CA78803), and Nycomed Amersham, Princeton, NJ. GSK thanks Dr. Dennis Fujii for many helpful discussions and Dr. Martin Lipton for advice and support.

Reference

1. Rinker-Schaeffer CW, Partin AW, Isaacs WB, Coffey DS, Isaacs JT. Molecular and cellular changes associated with the acquisition of metastatic ability by prostatic cancer cells. Prostate 1994;25:249-265.
2. Garnick M. The dilemmas of prostate cancer. Scientific American 1994:52 -59.
3. Moody-Ayers SY, Wells CK, Feinstein AR. 'Benign' tumors and 'early detection' in mammography-screened patients of a natural cohort with breast cancer. Arch Intern Med ;160:1109-1115.
4. Frouge C, Guinebretier J-M, Contesso G, Di Paola R, Blery M. Contrast Enhancement in Dynamic Magnetic Resonance Imaging of the Breast and Tumor Angiogenesis. Investigative Radiology 1994;29:1043-1049.
5. Furman-Haran E, Margalit R, Grobgeld D, Degani H. Dynamic contrast-enhanced magnetic resonance imaging reveals stress- induced angiogenesis in MCF7 human breast tumors. Proc Natl Acad Sci U S A 1996;93:6247-6251.
6. Heywang S, Hahn D, Schmidt H. Magnetic Resonance Imaging of the Breast Using Gd-DTPA. J Comput Assist Tomogr 1986;10:681-686.
7. Pham CD, Roberts TP, van Bruggen N, Melnyk O, Mann J, Ferrara N, Cohen RL, Brasch RC. Magnetic resonance imaging detects suppression of tumor vascular permeability after administration of antibody to vascular endothelial growth factor. Cancer Invest 1998;16:225-230.
8. Dixon WT. Simple Proton Spectroscopic Imaging. Radiology 1984;153:189-194.
9. Glover GH. Multipoint Dixon Technique for Water and Fat proton and Susceptibility Imaging. Journal of Magnetic Resonance Imaging 1991;1:521-530.

10. Hilaire L, Wehrli FW, Song HK, Hopkins JA. High-speed spectroscopic imaging at 4T for R2* measurement of individual spectral components. International Society for Magnetic Resonance in Medicine 1999:257.

11. Oikawa H, Al-Hallaq HA, Lewis MZ, River JN, Kovar DA, Karczmar GS. Spectroscopic imaging of water resonance with short repetition time to study tumor response to hyperoxia. Magn. Reson. Med. 1997;38:27-32.

12. Kovar DA, Al-Hallaq HA, Zamora MA, River JN, Karczmar GS. Fast spectroscopic imaging of water and fat resonances to improve the quality of MR images. Acad Radiol 1998;5:269-275.

13. Sarkar S, Heberlein K, Metzger GJ, Zhang X, Hu X. Applications of high-resolution echoplanar spectroscopic imaging for structural imaging. J Magn Reson Imaging 1999;10:1-7.

14. Al-Hallaq HA, Zamora M, Fish BL, Farrell A, Moulder JE, Karczmar GS. MRI measurements correctly predict the relative effect of tumor oxygenating agents on hypoxic fraction in rodent BA1112 tumors. Int J Radiat Oncol Biol Phys 2000;in press.

15. Kuperman V, River JN, Karczmar GS. Chemical Shift Imaging Study of Tumor Response to Hyperoxia. International Society for Magnetic Resonance in Medicine 1994;3:1333.

16. Karczmar GS, Fan X, Al-Hallaq HA, Zamora M, River JN, Rinker-Schaeffer C, Zaucha M, Tarlo K, Kellar K. Uptake of a Superparamagnetic Contrast Agent Imaged by MR with High Spectral and Spatial Resolution. Magnetic Resonance in Medicine 2000;43:633-639.

17. Karczmar GS, Fan X, Al-Hallaq H, River JN, Tarlo K, Kellar K, Zamora M, Rinker-Schaeffer C, Lipton MJ. Functional and Anatomic Imaging of Tumor Vasculature: High

Resolution MR Spectroscopic Imaging Combined with a Superparamagnetic Contrast Agent. Academic Radiology 2000;in press.

18. Karczmar GS, V.Y. K, Lewis MZ, River JN, Lubich L, Halpern H. High Resolution Spectroscopic Images of Tumors. ISMRM 1995.

19. Tennant TR, Kim H, Sokoloff M, Rinker-Schaeffer CW. The dunning model. Prostate ;43:295-302.

20. Lucia MS, Bostwick DG, Bosland M, Cockett AT, Knapp DW, Leav I, Pollard M, Rinker-Schaeffer C, Shirai T, Watkins BA. Workgroup I: rodent models of prostate cancer. Prostate 1998;36:49-55.

21. Kellar KE, Fujii DK, Gunther WH, Briley-Saebo K, Bjornerud A, Spiller M, Koenig SH. NC100150 Injection, a preparation of optimized iron oxide nanoparticles for positive-contrast MR angiography. J Magn Reson Imaging 2000 May;11:488-494.

22. Brown TR, Kincaid BM, Ugurbil K. NMR chemical shift imaging in three dimensions. Proc Natl Acad Sci U S A 1982;79:3523-3526.

23. Maudsley AA, Hilal SK, Perman WH, Simon HE. Spatially resolved high resolution spectroscopy by "four-dimensional" NMR. Journal of Magnetic Resonance 1983;51:147-152.

24. Fan X, River JN, Zamora M, Rinker-Schaeffer C, Karczmar GS. Calculation of pure absorption images from spectroscopic data increases image contrast and resolution. International Society for Magnetic Resonance im Medicine 1999.

25. Bauer WR, Hiller KH, Roder F, Rommel E, Ertl G, Haase A. Magnetization exchange in capillaries by microcirculation affects diffusion-controlled spin-relaxation: a model which describes the effect of perfusion on relaxation enhancement by intravascular contrast agents. Magn Reson Med 1996;35:43-55.

26. Shuter B, Wang SC, Roche J, Briggs G, Pope JM. Relaxivity of Gd-EOB-DTPA in the normal and biliary obstructed guinea pig. J Magn Reson Imaging 1998;8:853-861.

27. Kuhl CK. MRI of breast tumors. Eur Radiol ;10:46-58.

28. Posse S, Tedeschi G, Risinger R, Ogg R, Le Bihan D. High speed 1H spectroscopic imaging in human brain by echo planar spatial-spectral encoding. Magn Reson Med 1995;33:34-40.

29. Doyle M, Mansfield P. Chemical Shift Imaging: A Hybrid Approach. Magnetic Resonance in Medicine 1987;5:255-261.

30. Mansfield P. Spatial Mapping of the Chemical Shift in NMR. Magnetic Resonance in Medicine 1984;1:370-386.

Table 1. Summary of the tumor growth rate, tumor area, relative surface area (S_r), average intensity ratio of tumor to muscle (I_r), and the average maximum T_2^* changes in tumor and muscle before and just after injection of contrast agent. ΔT_2^* was calculated using only those pixels in which T_2^* decreased.

	Tumor growth rate (cm^3/day)	Imaging tumor area (cm^2)	Relative surface area of interior & entire tumor (S_r)	Intensity ratio of interior & entire tumor to muscle (I_r)	Average max T_2^* change for tumor & muscle (ms)
Non-Metastatic Tumors					
1	0.05	0.87	2.77 & 4.35	1.61 & 1.42	8.20 & 2.84
2	0.07	0.50	4.32 & 7.62	2.01 & 1.76	6.77 & 3.53
3	0.03	0.50	4.12 & 6.40	1.72 & 1.45	1.37 & 2.44
4	0.05	1.11	1.13 & 1.36	0.75 & 0.64	1.71 & 2.18
5	0.01	0.23	4.34 & 7.28	1.91 & 1.58	6.18 & 1.92
6	0.20	0.45	4.53 & 10.93	2.64 & 2.07	3.67 & 2.54
7	0.10	0.68	3.10 & 5.91	1.83 & 1.52	4.52 & 2.61
8	0.10	0.57	4.49 & 9.05	2.02 & 1.63	9.09 & 2.58
9	0.14	1.19	4.15 & 5.78	1.99 & 1.73	9.08 & 2.53
10	0.02	1.06	3.99 & 6.90	1.78 & 1.41	2.20 & 3.00
11	0.04	2.05	1.71 & 3.07	1.30 & 1.22	1.78 & 1.55
12	0.03	1.03	2.71 & 3.52	0.97 & 0.98	2.67 & 2.52
Metastatic Tumors					
1	0.12	1.21	4.33 & 5.36	1.96 & 1.70	2.06 & 3.08
2	0.06	0.48	5.26 & 3.81	1.38 & 1.04	2.66 & 2.61
3	0.04	0.50	4.77 & 5.45	1.28 & 1.16	3.55 & 3.14
4	0.14	1.05	4.08 & 5.71	1.64 & 1.52	0.92 & 2.98
5	0.25	1.27	6.33 & 8.19	2.19 & 1.81	2.93 & 1.90
6	0.03	1.34	7.58 & 10.34	2.50 & 1.76	2.70 & 1.08
7	0.07	1.67	11.40 & 10.69	2.01 & 1.60	5.09 & 2.72
8	0.15	1.60	8.55 & 9.94	2.04 & 1.76	4.69 & 4.35
9	0.21	1.30	17.86 & 17.87	2.95 & 2.26	3.03 & 7.36
10	0.05	0.60	5.36 & 6.76	1.52 & 1.30	4.48 & 2.47
11	0.11	2.42	6.72 & 7.27	1.55 & 1.41	3.72 & 1.51
12	0.04	0.99	5.15 & 5.37	1.45 & 1.24	2.06 & 2.09

Table 2. Average values of parameters with standard errors of the means for non-metastatic and metastatic tumors.

Calculated Parameter	Non-Metastatic Tumor		Metastatic Tumor	
	No contrast agent	With contrast agent	No contrast agent	With contrast agent
†S_r(interior tumor)	3.45±0.33	4.84±0.63	7.28±1.13	9.59±0.93
S_r(entire tumor)	6.01±0.77	7.20±1.17	8.06±1.10	10.24±0.95
†S_r(tumor rim)	2.6±0.5	2.4±0.6	0.8±0.3	0.6±0.5
I_r(interior tumor)	1.71±0.15	1.66±0.16	1.87+0.14	2.03±0.15
I_r(entire tumor)	1.45±0.11	1.37±0.11	1.55±0.10	1.65±0.11
†T_2^*(tumor) early changes	4.77±0.86		3.16+0.35	
T_2^*(muscle) early changes	2.52±0.15		2.94±0.47	
†S_{rdiff}(interior tumor)	40.83±5.26		158.33±58.31	
†S_{rdiff}(entire tumor)	52.17±6.70		141.64±48.52	
A_r	1.78±0.12		1.98+0.23	

†The parameters for metastatic and non-metastatic tumors were significantly different.

FIGURE CAPTIONS:

Figure 1. Images of non-metastatic tumors: (A) control peak height images, (B) edge enhanced images, and (C) difference images ('first image after contrast media injection' minus 'control images before contrast injection').

Figure 2. Metastatic tumors: (A) control peak height images, (B) edge enhanced images, and (C) difference images ('first image after contrast media injection' minus 'control images before contrast injection').

Figure 3. Image texture, S_r (arbitrary units) in tumor interiors for metastatic and non-metastatic tumors; S_r before contrast media injection is plotted against S_r after contrast media injection. The manually chosen dotted line suggests the optimal separation between the two tumor populations.

Figure 4. Image texture, S_r (interior) measured after contrast media injection plotted against $\sim S_r$(tumor rim) measured before contrast media injection. The manually chosen dotted line suggests the optimal separation between the two tumor populations.

Figure 5. Image texture, S_r over the interior of tumor after contrast agent injection as a function of the average maximum T_2^* changes over tumor just after injection of contrast agent. The manually chosen dotted line suggests the optimal separation between the two tumor populations.

Figure 1

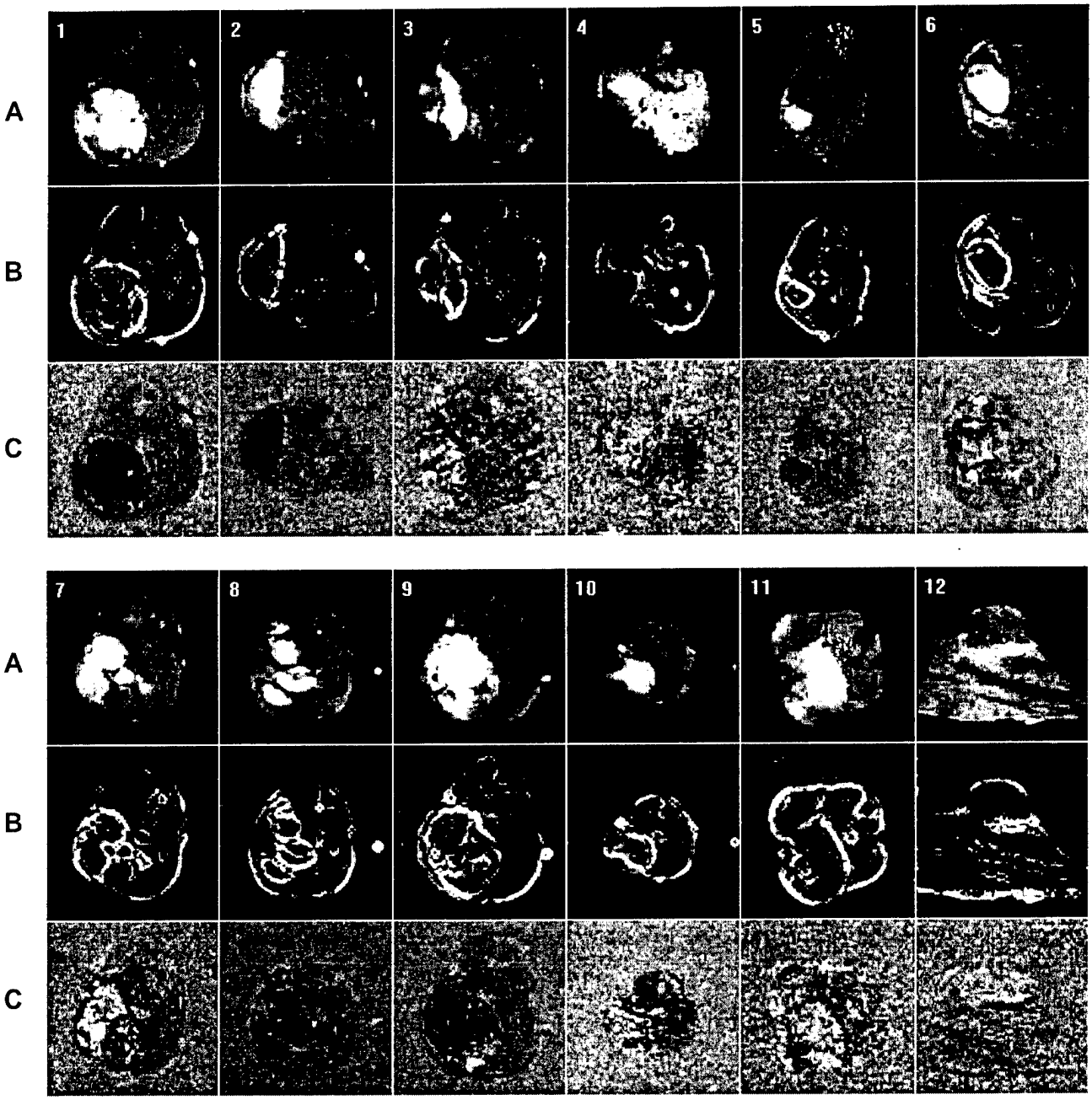

Figure 2

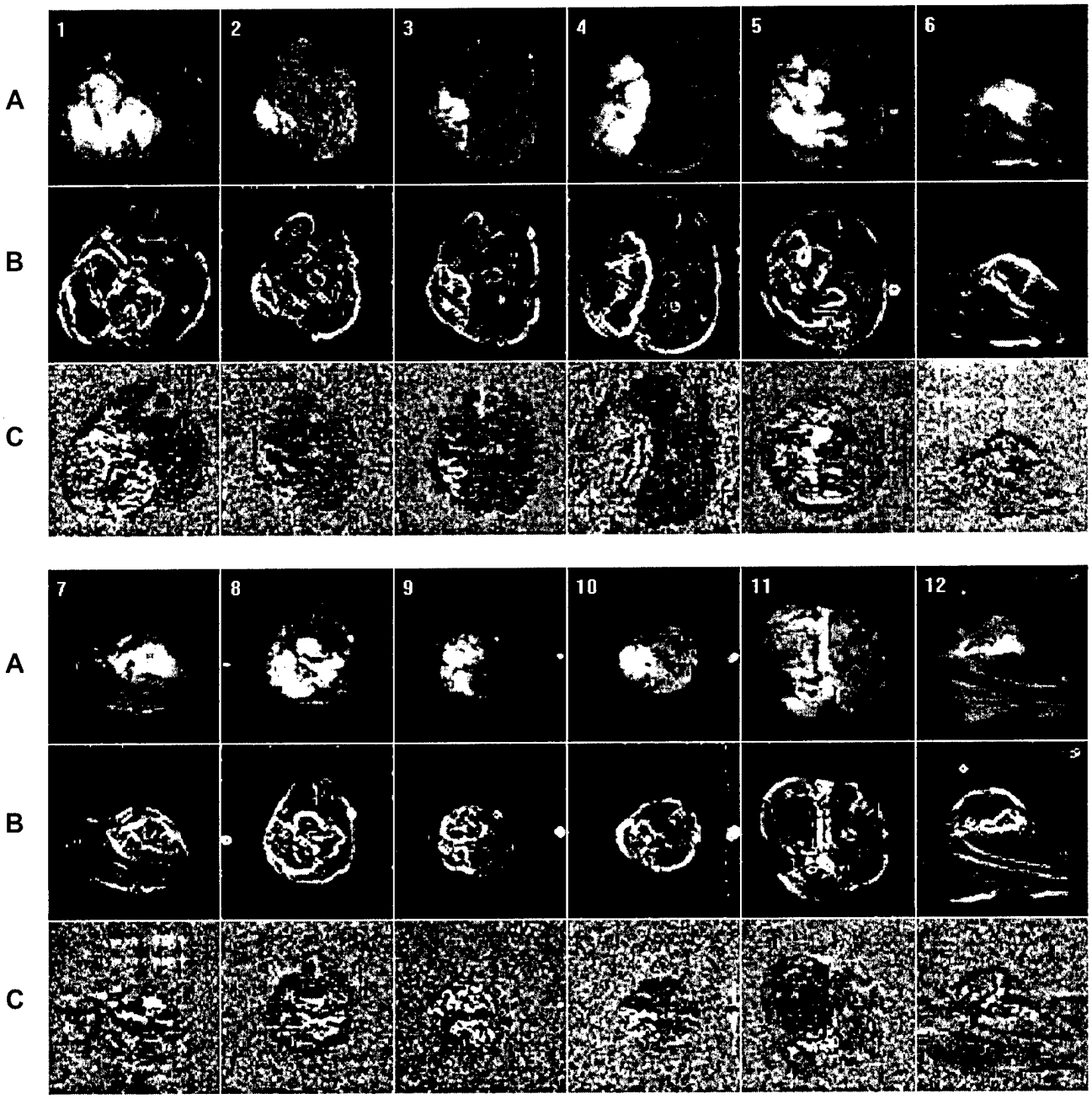

Figure 3

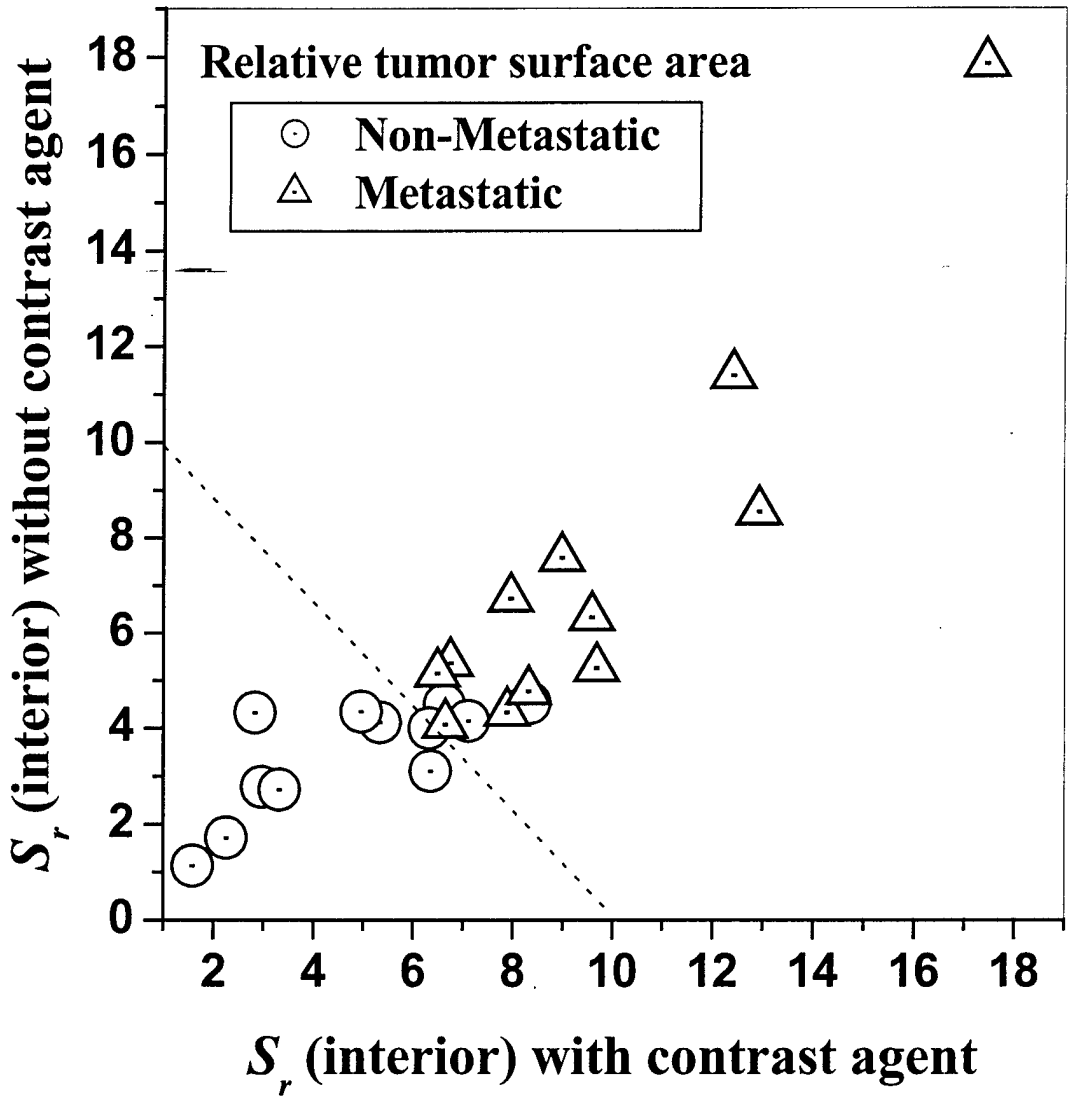
Relative tumor surface area
Non-Metastatic
Metastatic
S_r (interior) without contrast agent
S_r (interior) with contrast agent
0
2
4
6
8
10
12
14
16
18

Figure 4

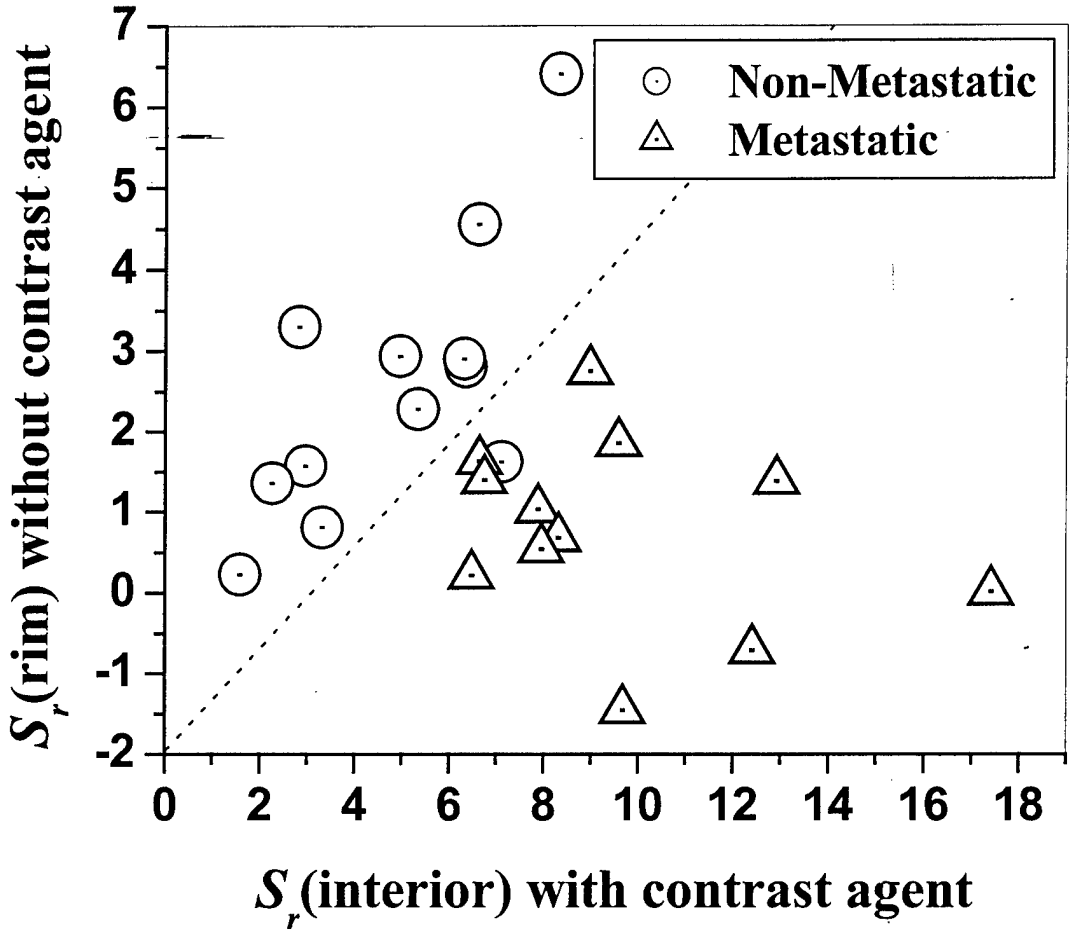
Non-Metastatic
Metastatic
S_r(rim) without contrast agent
S_r(interior) with contrast agent
7
6
5
4
3
2
1
0
-1
-2
0
2
4
6
8
10
12
14
16
18

Figure 5

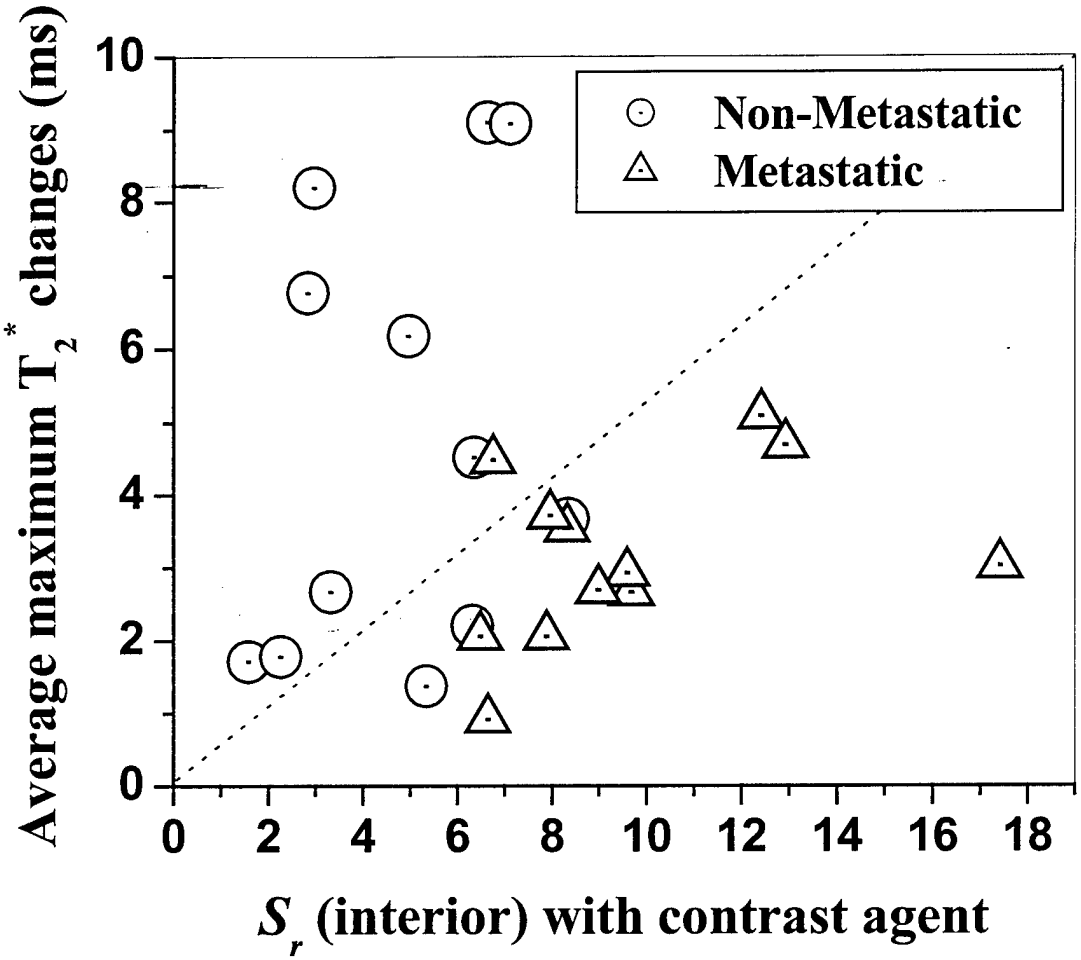
Average maximum T_2^* changes (ms)
S_r (interior) with contrast agent
Non-Metastatic
Metastatic
0
2
4
6
8
10
12
14
16
18